KSME

Springer

Journal of Mechanical Science and Technology 34 (6) 2020

Original Article
DOI 10.1007/s12206-020-0527-3

Keywords:
· Niemann worm wheel
· Side milling
· Numerical control machining
· Modelling
· Tooth profile modification
· Machining simulation

Correspondence to:
Quanping Sun
sunqp@hyit.edu.cn

Citation:
Wu, H., Zhang, Z., Sun, Q. (2020). High-efficiency technique for five-axis side milling of niemann worm wheels. Journal of Mechanical Science and Technology 34 (6) (2020) 2515~2524.
http://doi.org/10.1007/s12206-020-0527-3

Received July 27th, 2019
Revised February 27th, 2020
Accepted March 17th, 2020

† Recommended by Editor
Hyung Wook Park

High-efficiency technique for five-axis side milling of niemann worm wheels

Haibing Wu[1], Zheng Zhang[2] and Quanping Sun[1]

[1]Jiangsu Key Laboratory of Advanced Manufacturing Technology, Huai'an 223001, China, [2]School of Mechanical and Power Engineering, Nanjing Tech University, Nanjing 211800, China

Abstract Five-axis side milling technique for Niemann worm wheel teeth flank using a tapered flat-end mill is presented. Equations describing the worm wheel tooth flank were derived based on differential geometry and the working principle of gears. The tooth flank was modified by offsetting its point cloud computed using these equations along the normal direction. The maximum normal curvature of the worm wheel tooth flank was computed, and its minimum radius of curvature was obtained. The cutter path step length and spacing between cutter travels were computed to generate a uniform path for five-axis machining. Software simulations of the cutter path were performed for validation and for analysing errors in the worm wheel tooth flank machining; this technique was also verified by milling worm wheels. The results demonstrated that the technique not only improved machining efficiency by 5 times compared with point milling but also guaranteed precision machining of the tooth flank for five-axis machining of cylindrical worm drives.

1. Introduction

Compared with normal cylindrical worm drives, the Niemann worm drive offers higher transmission accuracy and efficiency and a longer service life. It is now widely used in metallurgy, mining, environmental protection, and the aerospace industry.

Before the five-axis CNC machining came into being, worm wheels could only be hobbed by the generating method with a hob on a gear hobbing machine [1, 2]. The hobbing process has higher efficiency, but the manufacturing cycle of the hob is relatively long, and the cost is considerably high. This method is suitable for mass production but not for single production. Five-axis CNC machining is highly flexible and has the benefit of low cost in small-batch production. This study proposes an efficient and high-precision five-axis CNC machining method for single-piece and small-batch production of Niemann worm wheels [3-13]. Table 1 shows a comparison of five-axis CNC machining and hobbing.

The tooth flank of the Niemann worm wheel is an extremely complex surface [14, 15]. Complex surfaces are now usually point-milled using ball-end mills, which is a low-efficiency and high-cost solution [16-18]. Five-axis side milling is a much more efficient method than point milling, but side milling requires the surface to be a ruled surface (such as a ruled-surface impeller face) or at least one of the U and V directions of the surface to be convex (the U and V directions of the non-ruled-surface impeller back are concave). The Niemann worm wheel has a convex shape in the tooth height direction. Therefore, this paper proposes a method for machining the tooth flank of a Niemann worm wheel by side milling using a tapered flat-end mill, which can considerably improve the machining efficiency of the tooth flank on the premise of

Table 1. Comparison of five-axis CNC machining and hobbing.

Method	Applicable situation	Tool cost	Machining time
Hobbing	Mass production	358 $	2 h
Five-axis CNC machining	Small-batch production	41 $	2.5 h

controlling tooth surface error. The feasibility of the technique was verified through milling simulation and trial applications. This technique provides a new solution for worm wheel machining in small-batch manufacturing.

2. Worm drive modelling and tooth profile modification

2.1 Equations describing worm shaft tooth flank

Fig. 1 illustrates the motion of a worm and grinding wheel set. Here, $O_uX_uY_uZ_u$ represents the coordinate system for the grinding wheel, OXYZ denotes the fixed co-ordinate system, $O_1X_1Y_1Z_1$ represents the coordinate system for the worm, θ is the rotation angle of the worm coordinate system relative to the fixed coordinate system, p is the axial travel resulting from the worm's rotation by a unit radian, γ is the lead angle at the reference cylinder of the worm, and a_1 is the distance between the centres of the grinding wheel and the worm. With the parameters illustrated in Fig. 1, the following matrix for converting the grinding wheel coordinate system to the worm coordinate system can be derived:

$$M_{1u} = M_{10}M_{0u} = \begin{bmatrix} \cos\theta & \sin\theta\cos\gamma & -\sin\theta\cos\gamma & a_1\cos\theta \\ -\sin\theta & \cos\theta\cos\gamma & -\cos\theta\sin\gamma & -a_1\cos\theta \\ 0 & \sin\gamma & \cos\gamma & -p\theta \\ 0 & 0 & 0 & 1 \end{bmatrix} \tag{1}$$

where M_{ou} is the matrix for converting the grinding wheel coordinate system to the fixed coordinate system and M_{10} is the matrix for converting the fixed coordinate system to the worm coordinate system.

Combining Figs. 1~3, the following equation can be derived for describing the cutting surface of the grinding wheel:

$$\begin{cases} x_u = -(p\sin\beta + c)\cos\psi \\ y_u = (p\sin\beta + c)\sin\psi \\ z_u = p\cos\beta - d \end{cases} \tag{2}$$

where β and ψ are parameters defining the cutting surface of the grinding wheel, c is the distance from the centre of the cutting surface of the grinding wheel to the axis of rotation of the grinding wheel, and d is the axial distance from the axis of rotation of the grinding wheel to the centre of the cutting surface of the grinding wheel, as illustrated in Figs. 1~3.

The motion of the grinding wheel cutting the worm is an enveloping motion, which satisfies the following equation for the meshing of conjugate surfaces:

$$\vec{v}_{u1} \cdot \vec{n}_u = 0 \tag{3}$$

where $\vec{v}_{u1}$ is the velocity vector of the motion of the grinding wheel relative to the worm and $\vec{n}_u$ is the normal vector at the point of contact for the grinding wheel and worm.

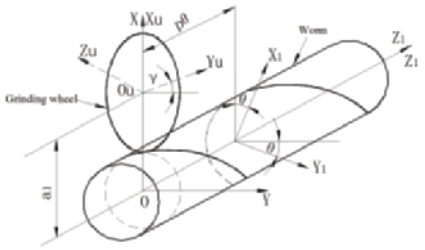

Fig. 1. Illustration of motion of a grinding wheel and worm set.

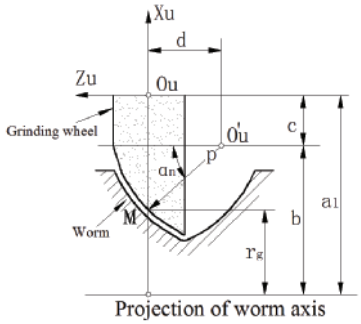

Fig. 2. Illustration of axial section of grinding wheel.

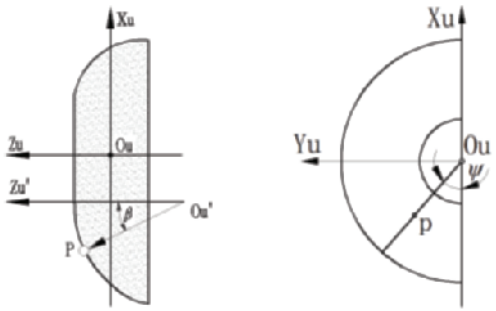

(a) (b)

Fig. 3. Illustration of cutting surface of grinding wheel: (a) Axial sectional view; (b) transverse sectional view.

Thus, the contact between the grinding wheel and worm can be described using the following equation:

$$\tan\beta = \left(c\cos\psi - a_1 + p\cot\gamma\right) / \left(-k\cos\psi + a_1\sin\psi\cot\gamma + p\sin\psi\right). \tag{4}$$

The following equation can then be derived for describing the worm tooth flank, by transforming Eq. (2) into the worm coordinate system using Eq. (1) and simultaneously solving Eqs. (2) and (4):

$$\begin{cases} x_1 = a_1\cos\theta - \cos\psi\cos\theta(c + p\sin\beta) + \sin\gamma\sin\theta(d - p\cos\beta) \\ \quad + \cos\gamma\sin\psi\sin\theta(c + p\sin\beta) \\ y_1 = \cos\theta\sin\gamma(d - p\cos\beta) - a_1\sin\theta + \cos\psi\sin\theta(c + p\sin\theta) \\ \quad + \cos\gamma\cos\theta\sin\psi(c + p\sin\beta) \\ z_1 = \sin\gamma\sin\psi(c + p\sin\theta) - \cos\gamma(d - p\cos\beta) - p\theta \\ \beta = \tan^{-1}\dfrac{-a_1 - p\cot\gamma + c\cos\psi}{-k\cos\psi + a_1\sin\psi\cot\gamma + p\sin\psi}. \end{cases} \tag{5}$$

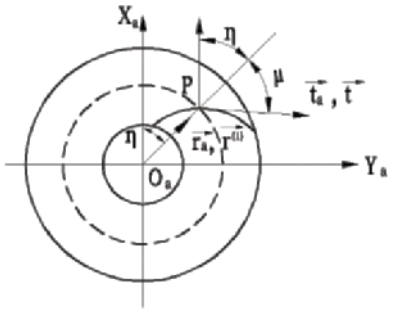

Fig. 4. Transverse profile of worm.

Eq. (5) essentially represents the complex spiral path of contact (a three-dimensional line) between the grinding wheel and the worm. The tooth flank of the worm is formed by rotating the transverse profile of the worm spirally around the axis of rotation of the worm. As the transverse profile is two-dimensional, describing the worm tooth flank in this manner yields a simpler numerical representation. Designating $z_1 = 0$ in Eq. (5), the following equation can be derived for describing the transverse profile of worm:

$$\begin{cases} x_1 = a_1\cos\theta - \cos\psi\cos\theta(c + p\sin\beta) + \sin\gamma\sin\theta(d - p\cos\beta) \\ \quad + \cos\gamma\sin\psi\sin\theta(c + p\sin\beta) \\ y_1 = \cos\theta\sin\gamma(d - p\cos\beta) - a_1\sin\theta + \cos\psi\sin\theta(c + p\sin\theta) \\ \quad + \cos\gamma\cos\theta\sin\psi(c + p\sin\beta) \\ \theta = \sin\gamma\sin\psi(c + p\sin\theta) - \cos\gamma(d - p\cos\beta)/p \\ \beta = \tan^{-1}\dfrac{-a_1 - p\cot\gamma + c\cos\psi}{-k\cos\psi + a_1\sin\psi\cot\gamma + p\sin\psi}. \end{cases} \quad (6)$$

Fig. 4 illustrates the transverse profile of the worm. Here, $O_aX_aY_aZ_a$ denotes the coordinate system for the transverse profile of worm. With the parameters illustrated in Fig. 4, the following equation can be derived for describing the transverse profile of the worm:

$$\begin{cases} x_a = r^{(1)}\cos(\eta) \\ y_a = r^{(1)}\sin(\eta) \\ z_a = 0. \end{cases} \quad (7)$$

As the tooth flank is taken to be formed by rotating the transverse profile of the worm spirally around the axis of rotation of the worm, numerical representation of the worm can be simplified as:

$$\begin{cases} x_1 = r^{(1)}\cos(\eta + \zeta) \\ y_1 = r^{(1)}\sin(\eta + \zeta) \\ z_1 = p\zeta. \end{cases} \quad (8)$$

In Eqs. (7) and (8), ζ is the circumferential angle of the spiral rotation of the transverse profile of worm around the axis of worm. Here, $r^{(1)}$ is the length of the radius vector of the transfer tooth profile , η is the intersection angle of $\vec{r}^{(1)}$ and Xa, and μ is the intersection angle of $\vec{r}^{(1)}$ and Ya. These parameters can be obtained using the following equation:

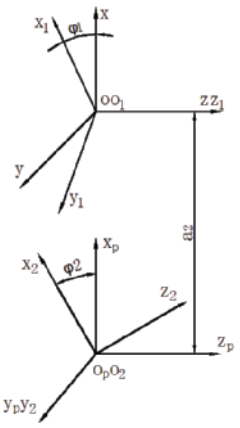

Fig. 5. Coordinate systems for a meshed worm and worm wheel set.

$$\begin{cases} \vec{r}^{(1)} = \sqrt{x_1^{\,2} + y_1^{\,2}} \\ \eta = \arctan(y_1 / x_1) \\ \mu = \pi/2 - \eta + \arctan(n_{y_1} / n_{x_1}) \end{cases} \quad (9)$$

where n_{y_1} and n_{x_1} are the normal vectors of the transverse profile of the worm. Eq. (9) shows that $\vec{r}^{(1)}$, η, and μ are functions of ψ. Therefore, the independent parameters of Eq. (8) are ψ and ζ.

2.2 Equations for describing worm wheel tooth flank

Fig. 5 shows the coordinate systems for a meshed worm and worm wheel set. Here, $O_1X_1Y_1Z_1$ refers to the coordinate system for the worm, OXYZ denotes the fixed coordinate system for the worm, $O_PX_PY_PZ_P$ represents the fixed coordinate system for the worm wheel, $O_2X_2Y_2Z_2$ constitutes the coordinate system for the worm wheel, a_2 is the distance between the centres of the worm and worm wheel, and φ_1 and φ_2 are the rotation angles of the worm and worm wheel, respectively.

With the parameters illustrated in Fig. 5, the following matrix can be derived for transforming the worm coordinate system to the worm wheel coordinate system:

$$\begin{bmatrix} x_2 \\ y_2 \\ z_2 \end{bmatrix} = M_{2P}(M_{p0} + M_{01}\begin{bmatrix} x_1 \\ y_1 \\ z_1 \end{bmatrix}) \quad (10)$$

where

$$M_{01}=\begin{bmatrix}\cos\varphi_1 & -\sin\varphi_1 & 0\\ \sin\varphi_1 & \cos\varphi_1 & 0\\ 0 & 0 & 1\end{bmatrix}, M_{p0}=\begin{bmatrix}a\\0\\0\end{bmatrix}, M_{2P}=\begin{bmatrix}\cos\varphi_2 & 0 & -\sin\varphi_2\\ 0 & 1 & 0\\ \sin\varphi_2 & 0 & \cos\varphi_2\end{bmatrix}.$$

The worm wheel tooth flank is enveloped by the worm tooth flank and satisfies the following equation for the meshing of conjugate surfaces:

$$\vec{v}_{12}\cdot\vec{n}_1=0 \tag{11}$$

where $\vec{v}_{12}$ is the velocity vector of the motion of the worm relative to the worm wheel, and $\vec{n}_1$ is the normal vector at the contact point of the worm and worm wheel.

Then, the contact between the worm and worm wheel can be described using the following equation:

$$r^{(1)}\left[r^{(1)}\cos(\eta+\zeta+\varphi_1)+a_2-\frac{p}{i_{21}}\right]\cos\mu-p^2\zeta\sin(\eta+\zeta+\mu+\varphi_1)=0. \tag{12}$$

With Eqs. (8), (10) and (12) resolved simultaneously, the following equation can be obtained for describing the worm wheel tooth flank:

$$\begin{cases} r^{(1)}\left[r^{(1)}\cos(\eta+\zeta+\varphi_1)+a_2-\frac{p}{i_{21}}\right]\cos\mu-p^2\zeta\sin(\eta+\zeta+\mu+\varphi_1)=0\\ x_1=r^{(1)}\cos(\eta+\zeta)\\ y_1=r^{(1)}\sin(\eta+\zeta)\\ z_1=p\zeta\\ x_2=\cos(i_{21}\varphi_1)(a+x_1\cos\varphi_1-y_1\sin\varphi_1)-z_1\sin(i_{21}\varphi_1)\\ y_2=y_1\cos\varphi_1+x_1\sin\varphi_1\\ z_2=\sin(i_{21}\varphi_1)(a+x_1\cos\varphi_1-y_1\sin\varphi_1)+z_1\cos(i_{21}\varphi_1). \end{cases} \tag{13}$$

Eq. (13) yields a line of contact between the worm and the worm wheel for a given value of φ_1. With iteration of ψ and ζ performed according to their respective ranges of values, the point set of the line of contact for a given moment can be obtained. The point cloud of the entire worm wheel flank can then be obtained by repeating the steps above to compute the set of lines of contact between the worm and the worm wheel.

2.3 Worm wheel tooth profile modification

The centre of the contact area of a meshed worm drive set can be determined according to the requirements regarding the area and position of the contact between meshed worm drive sets provided in relevant standards and handbooks. The centre is the reference point (O_c) for modifying the worm wheel tooth profile. First, a plane that is tangential to the worm wheel tooth flank and crosses the reference point needs to be established. Next, a coordinate system for the tangential plane, $O_CX_CY_C$, needs to be established with the reference point as the origin (O_c), the tooth width direction as the X_C-axis, and the tooth depth direction as the Y_C-axis.

Projecting the point in the tooth facing the tangential plane, the coordinates of the projection in the tangential plane can be expressed as:

$$\begin{cases} x_{proj}=(x-x_c)i_{xc}+(y-y_c)j_{xc}+(z-z_c)k_{xc}\\ y_{proj}=(x-x_c)i_{yc}+(y-y_c)j_{yc}+(z-z_c)k_{yc} \end{cases} \tag{14}$$

where x_{proj} and y_{proj} are the coordinates of the projection in the tangential plane; x, y, and z are the coordinates of the point before the projection; x_c, y_c, and z_c are the coordinates of the reference point for tooth profile modification; i_{xc}, j_{xc}, and k_{xc} are the unit vectors of the X_C-axis of the coordinate system for the tangential plane; and i_{yc}, j_{yc}, and k_{yc} are the unit vectors of the Y_C-axis of the coordinate system for the tangential plane.

The offset of tooth flank (*dis*) can then be solved by substituting Eq. (14) into the following equation:

$$dis=A\cdot x_{proj}^2+B\cdot y_{proj}^2 \tag{15}$$

where

$$A=dis_{cont}/(k_{t1}\cdot st)^2$$
$$B=dis_{cont}/(k_{t2}\cdot h_a)^2$$

where dis_{cont} is the reference distance between the contact points of a meshed worm and worm wheel set, k_{t1} is the ratio of the length of the contact area to the tooth width of the worm wheel, k_{t2} is the ratio of the width of the contact area to the tooth depth of the worm wheel, and st and h_a are the tooth width and depth of the worm wheel, respectively.

The coordinates of a point on the tooth flank after the offsetting can be computed by substituting Eq. (15) into the following equation:

$$\begin{cases} x_{\text{mod}}=x+dis\cdot n_{x_2}\\ y_{\text{mod}}=y+dis\cdot n_{y_2}\\ z_{\text{mod}}=z+dis\cdot n_{z_2} \end{cases} \tag{16}$$

where x_{mod}, y_{mod}, and z_{mod} are the coordinates of the point in the tooth flank after offsetting; x, y, and z are the coordinates of the point in the tooth flank before the offsetting; and, n_{x_2}, n_{y_2} and n_{z_2} are the unit normal vectors of the worm wheel tooth flank.

3. Algorithms for generating cutter contact point of side milling of worm wheel tooth flank

The minimum radius of normal curvature of the contact point (P_1) of a worm drive set cannot be directly resolved using the line defined by the equation for describing the contact included in Eq. (13), a transcendental trigonometric equation. In this

study, the maximum normal curvature and induced normal curvature in the principal direction ($K_{g1}^{(12)}$) of the contact point (P_1) in the worm surface were resolved according to the formation principle of conjugate surfaces. Then, the maximum normal curvature at the contact point (P_1) in the worm wheel surface was computed according to the definition of the induced normal curvature. Finally, the minimum radius of curvature at the contact point (P_1) in the worm wheel surface was obtained.

3.1 Solving minimum radius of curvature of worm wheel surface

Any contact point in the worm surface has two principal curvatures, which are unequal and are in different directions. Using calculus to resolve the extrema, the principal curvatures and principal directions can be expressed using the following equations:

$$\begin{aligned}&(EG-F^2)k_n^2-(EG-2FM+GL)k_n+(LN-M^2)=0\\&EM-FLe_g^{\ 2}+(EN-GL)e_g+(FN-GM)=0\end{aligned}\tag{17}$$

where E, F, G, L, M, and N are the first and second base quantities, k_n is the curvature, and $\vec{e}_{g1}$ is the principal direction.

Then, the maximum normal curvature (k_{gn}) and principal direction ($\vec{e}_{g1}$) at the contact point (P_1) can be obtained by solving Eqs. (8) and (17) simultaneously.

To obtain the induced normal curvature ($K_{g1}^{(12)}$), the first step was to compute the normal curvature and short-range torsion of the contact point in the worm surface in the direction of the relative velocity ($\vec{v}^{(12)}$) of the meshed worm and worm wheel set:

$$\begin{aligned}K_v^{(1)}&=K_v^{(u)}-K_v^{(u1)}\\G_v^{(1)}&=G_v^{(u)}-G_v^{(u1)}\end{aligned}\tag{18}$$

where $K_v^{(u)}$ and $G_v^{(u)}$ are the normal curvature and short-range torsion, respectively, of the point in the cutting surface of the grinding wheel in the $\vec{v}^{(12)}$ direction, and $K_v^{(u1)}$ and $G_v^{(u1)}$ are the induced normal curvature and induced short-range torsion, respectively, of the meshed grinding wheel and worm set.

The induced normal curvature ($K^{(12)}$) at the contact point (P_1) in the normal direction of the contact path can be obtained by substituting the values of $K_v^{(1)}$ and $G_v^{(1)}$ given by Eq. (18) into the following equation:

$$K^{(12)}=\frac{1}{\Psi^{(12)}}(a_{x1}^{\ 2}+a_{y1}^{\ 2}+a_{z1}^{\ 2})\tag{19}$$

where

$$\begin{aligned}\Psi^{(12)}=\vec{n}_1\cdot\left[\vec{\omega}^1\times(\vec{\omega}^2\times\vec{r}^{\,2})-\vec{\omega}^2\times(\vec{\omega}^1\times\vec{r}^{\,1})\right]\\+(\vec{\omega}^{12},\ \vec{n}_1,\ \vec{v}^{(12)})+K_v^{(1)}(\vec{v}^{(12)})^2\end{aligned}\tag{20}$$

$$\begin{cases}a_{x1}=K_v^{(1)}v_{x1}^{(12)}+G_v^{(1)}\left(n_{y1}v_{z1}^{(12)}-n_{z1}v_{y1}^{(12)}\right)\\\qquad+\left(-i_{21}n_{z1}\cos\varphi_1-n_{y1}\right)\\a_{y1}=K_v^{(1)}v_{y1}^{(12)}+G_v^{(1)}\left(n_{z1}v_{x1}^{(12)}-n_{x1}v_{z1}^{(12)}\right)\\\qquad+\left(i_{21}n_{z1}\sin\varphi_1+n_{x1}\right)\\a_{z1}=K_v^{(1)}v_{z1}^{(12)}+G_v^{(1)}\left(n_{x1}v_{y1}^{(12)}-n_{y1}v_{x1}^{(12)}\right)\\\qquad+\left(-i_{21}n_{y1}\sin\varphi_1+i_{21}n_{x1}\cos\varphi_1\right)\end{cases}\tag{21}$$

where $\vec{\omega}^1$, $\vec{\omega}^2$ are the angular velocities of the worm and worm wheel, respectively; $\vec{r}^{\,1}$ and $\vec{r}^{\,2}$ are the radius vectors of the contact point in the coordinate systems for the worm and worm wheel, respectively; $\vec{v}^{(12)}$ is the velocity of the worm relative to the worm wheel; and $\vec{n}_1$ is the normal vector at the contact point (P_1) in the worm surface.

Then, the induced normal curvature $K_{g1}^{(12)}$ at the contact point (P_1) in the maximum curvature direction $\vec{e}_{g1}$ can be obtained by substituting the value of $K^{(12)}$ into the following equation:

$$K_{g1}^{(12)}=K^{(12)}\cos\varphi_a\tag{22}$$

where φ_a is the contact angle from the normal direction ($\vec{\sigma}$) of the line of contact to the direction of the maximum normal curvature ($\vec{e}_{g1}$).

Then, the maximum normal curvature (k_{ln}) at the contact point (P_1) in the worm wheel surface can be obtained by substituting the values of k_{gn} and $K_{g1}^{(12)}$ into the following equation:

$$K_{g1}^{(12)}=k_{gn}-k_{ln}.\tag{23}$$

Finally, the minimum radius of curvature (R_n) can be obtained by substituting the value of k_{ln} in Eq. (24):

$$R_n=\frac{1}{k_{ln}}.\tag{24}$$

The minimum radius of curvature (R_n) at each contact point of the meshed worm and worm wheel set was computed using the method above. The minimum radius of curvature (R_{min}) for the entire worm wheel surface was then obtained through numerical comparison.

3.2 Discretization of worm wheel-cutter contact points

In this study, the cutter path was divided into uniform sections as follows. First, the machining tolerance (ε_s) was determined. Next, the cutting step length along the cutter path (L_S) was computed using Eq. (25). Next, the spacing between the travels of cutting path was computed using Eq. (26). Then, the cross-section of the worm wheel surface in the axial direction of the worm wheel (tooth width direction) at a distance of ≤ L_S was

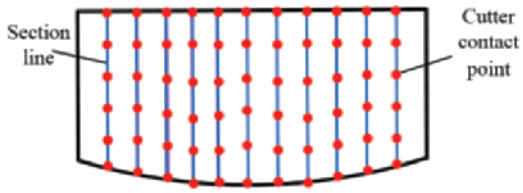

Fig. 6. Illustration of discretization of cutter contact points in worm wheel surface.

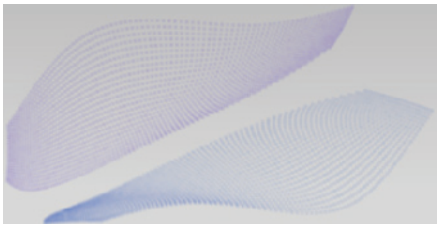

Fig. 7. Cutter contacts in worm wheel tooth flank.

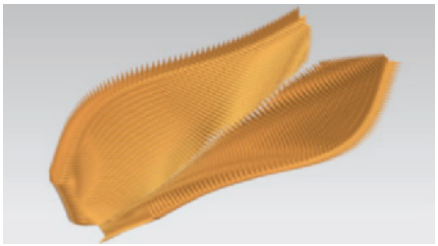

Fig. 8. Normal vectors at cutter contacts in worm wheel tooth flank.

determined. The longest cross-section was divided into equal sections with a length of $\leq \tau$ to obtain the number of discrete points. Finally, all the other cross-sections were divided into the same number of equal sections. Fig. 6 illustrates the procedure above.

$$L_S = 2\sqrt{\varepsilon_s(2R_{\min} - \varepsilon_s)} \tag{25}$$

$$\tau = 2R_{\min}\sqrt{1 - \left[\frac{R_{\min}}{R_{\min} + \varepsilon_s}\right]}. \tag{26}$$

In Fig. 6, the chamfering and gorge circle of the worm wheel tooth flank are neglected; the top line represents the tip; the bottom line represents the boundary between the flank and the root circle.

The coordinates of the cutter contact and the normal vector of toot flank at each cutter contact were retrieved on a three-dimensional CAD software, as shown in Figs. 7 and 8.

4. Computation of cutter path in worm wheel tooth flank

The coordinates of the cutter location points and the vector of the cutter shaft were computed according to the coordinates and normal vectors of the cutter contact points in the worm wheel tooth flank. To achieve uniform cutter wear, this study developed an algorithm for allowing the entire cutting edge of a tapered flat-end mill to participate in milling.

4.1 Computing the vector of cutter shaft

To control the oscillation angle of the cutter shaft, the generating line of conical surface of the cutter that crosses the cutter contact point should remain parallel to the transverse surface of worm wheel. Therefore, the vectors of the generating line $\vec{m}_u(u_m\ v_m\ w_m)$ are the cross products of the flank normal vector $\vec{n}_2(u_{n_2}\ v_{n_2}\ w_{n_2})$ and the unit vector of $+Z_2$-axis can be described as follows:

$$\begin{cases} u_m = v_{n_2} \\ v_m = -u_{n_2} \\ w_m = 0. \end{cases} \tag{27}$$

With the vector of the generating line, the normal vector at the cutter contact point in the tooth flank, and the half taper angle of the cutter already known, the components of the vector of cutter shaft can be obtained using the following equation:

$$\begin{cases} u = v_{n_2}\cos\Delta + u_{n_2}\sin\Delta\left(u_{n_2}{}^2 + v_{n_2}{}^2\right) \\ v = v_{n_2}\sin\Delta\left(u_{n_2}{}^2 + v_{n_2}{}^2\right) - u_{n_2}\cos\Delta \\ w = \sin\Delta\left(w_{n_2}u_{n_2}{}^2 + w_{n_2}v_{n_2}{}^2\right) \end{cases} \tag{28}$$

where Δ is the half taper angle of the cutter.

4.2 Computing cutter location point

Fig. 9 illustrates the method for obtaining the cutter location point. First, the discrete point P_1 is projected onto the cutter shaft along the normal vector of the tooth flank, with the projection point designated as P_{1t}. Next, point P_{1t} is projected onto the bottom surface of the cutter along the reverse direction of the vector of the cutter shaft. The resulting projection point C_0 is the cutter location point.

The coordinates of the projection point were computed using the following equation:

$$\begin{cases} x_{1t} = x_n + dev \cdot u_{n_2} \\ y_{1t} = y_n + dev \cdot v_{n_2} \\ z_{1t} = z_n + dev \cdot w_{n_2} \end{cases} \tag{29}$$

where x_{1t}, y_{1t}, and z_{1t} are the coordinates of the projection point; x_n, y_n, and z_n are the coordinates of the cutter contact point; *dev* is the distance from the cutter contact point to the projection point on the cutter shaft (along the normal vector of tooth flank) and is computed using the following equation:

$$dev = \left(\frac{(L_S - 2\cdot gap)}{(N_S - 1)(N_S - k_d) + gap + D/2\sin\Delta}\right)\tan\Delta + (D/2\cos\Delta) \tag{30}$$

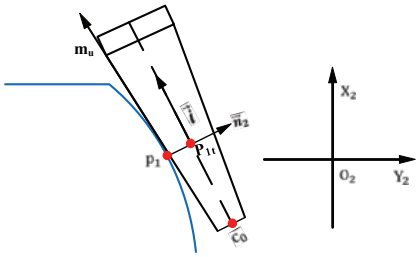

Fig. 9. Illustration of method for computing cutter location point.

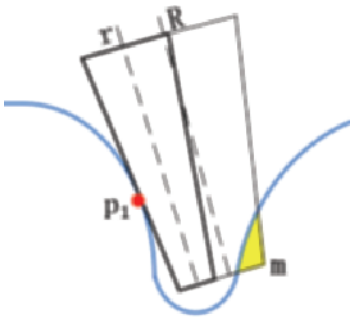

Fig. 10. Illustration of cutter interference.

The coordinates of the cutter location point were computed by substituting Eq. (29) into the following equation:

$$\begin{cases} x = x_{1t} - ((L_S - 2\cdot gap)/(N_S - 1)(N_S - k_d) + gap + D/2\sin\Delta)/u\cos\Delta \\ y = y_{1t} - ((L_S - 2\cdot gap)/(N_S - 1)(N_S - k_d) + gap + D/2\sin\Delta)/v\cos\Delta \\ z = z_{1t} - ((L_S - 2\cdot gap)/(N_S - 1)(N_S - k_d) + gap + D/2\sin\Delta)/w\cos\Delta \end{cases} \quad (31)$$

In Eqs. (30) and (31), L_S is the length of the cutting edge, *gap* is the allowance throughout the length of the cutting edge, N_S is the number of cutter travels, k_d is the sequential number of cutter travel, and D is the diameter of the cutter.

4.3 Interference verification and correction

As shown in Fig. 10, the worm wheel tooth flank consists of two opposite surfaces, and the end surface of the cutter while machining one of the surfaces may possibly interfere with the other surface. This validity of this possibility can be verified using the following equation:

$$\left|\vec{m} - \vec{c}_0\right|^2 - \left[(\vec{m} - \vec{c}_0)\cdot\vec{i}\right]^2 > r^2 \quad (32)$$

where $\vec{m}$ is the vector of coordinates at the point in the other surface of the tooth flank, $\vec{c}_0$ is the vector of coordinates at the cutter location point, $\vec{i}$ is the vector of cutter shaft, and r is the radius of the cutter. If the computation result does not satisfy the above equation, then there exists interference owing to the end surface of the cutter and a cutter with a smaller radius needs to be selected to eliminate the interference.

Table 2. Parameters for modelling and tooth profile modification of worm drive.

Parameter	Value	Parameter	Value
Modulus (mm)	10	Number of starts of worm	3
Number of teeth	31	Radius of the cutting surface of grinding wheel (mm)	56
Addendum modification coefficient of worm wheel	0.4	Lead angle of reference cylinder of worm (°)	20.1
Nominal pressure angle of grinding wheel (°)	23	Dedendum coefficient	1.2
Addendum coefficient	1	Maximum modification	0.2

Table 3. Parameters for worm wheel machining.

Parameter	Value	Parameter	Value
Cutter path step length (mm)	1.5	Spacing between travels of cutter path	0.63
Diameter of cutter (mm)	4	Cutting edge length (mm)	18
Half taper angle of cutter (°)	6	Effective cutting-edge length (mm)	10

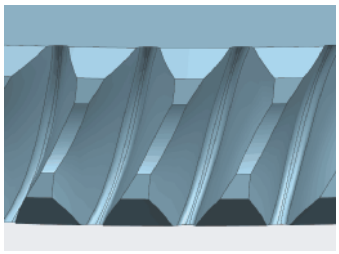

Fig. 11. Three-dimensional model for worm wheel tooth profile modification.

5. Trial applications for verifying five-axis milling of worm wheel tooth flank

5.1 Accurate three-dimensional modelling and tooth profile modification of worm wheel

Table 2 shows the parameters for the modelling and tooth profile modification of a three-start right-hand Niemann worm drive.

First, the point cloud for the modified worm wheel tooth flank was computed according to the modelling and tooth profile modification algorithm described in Sec. 1. Next, the tooth surface was simulated using the point cloud (tooth surface fitting accuracy is 0.0017 mm). Finally, the tooth profile of the blank worm wheel was modified using the simulated surface to obtain a three-dimensional model of the worm wheel, as shown in Fig. 11.

5.2 Simulation verification of the numerical-control side milling

Table 3 shows the parameters for machining the worm wheel (machining tolerance: 0.005 mm).

The coordinates and normal vector of the cutter location

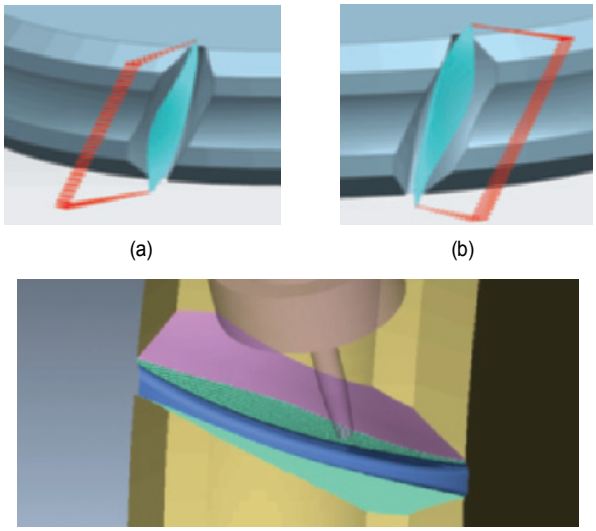

(a) (b) (c)

Fig. 12. Cutter path and simulation machining of worm wheel flank: (a) Cutter path for left-hand surface; (b) cutter path for right-hand surface; (c) simulation of worm wheel machining.

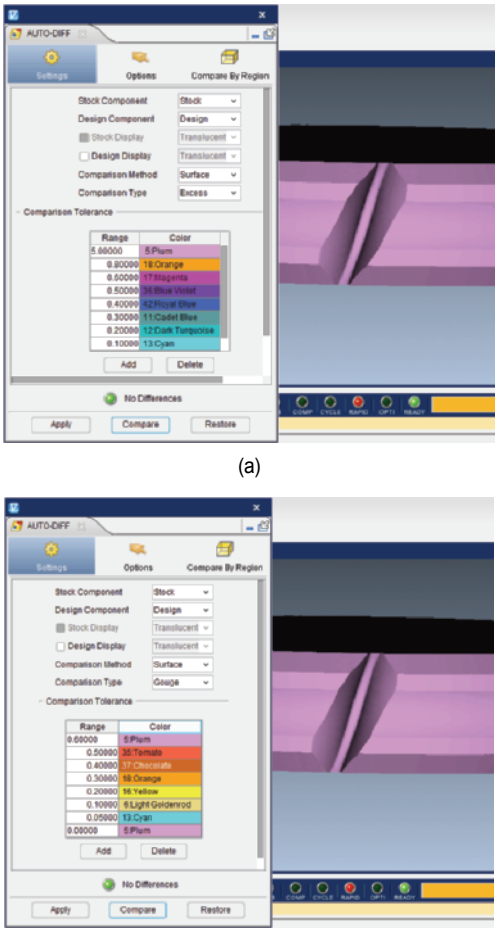

(a) (b)

Fig. 13. Accuracy analysis of simulation machining of worm wheel: (a) Overcut analysis; (b) under-cut analysis.

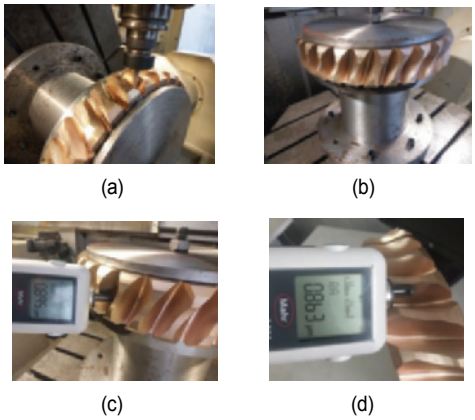

(a) (b) (c) (d)

Fig. 14. Worm wheel products and surface roughness measurements: (a) Finished side-milled worm wheel; (b) finished worm wheel; (c) measuring roughness in the direction of tooth depth; (d) measuring roughness in the direction of tooth width.

Fig. 15. Meshing contact spots left by the meshing test.

point were obtained according to the algorithm described in Sec. 3, with the resulting cutter location points exported as a cutter location file. The file was then processed to generate G codes, which were then input into the VERICUT software to perform simulation analysis, as shown in Fig. 12.

The worm wheel tooth flank obtained from the simulation machining in the VERICUT program was compared with that obtained by the three-dimensional design model, as shown in Fig. 13.

The comparative analysis results confirmed no over- or under-cutting.

5.3 Milling test

Worm wheels (tin bronze) were machined using a five-axis numerical-control machine (MIKRON UCP 800 Duro). The spindle speed was 8000 r/min, and the feed speed was 1500 mm/min. The resulting products had a roughness of approximately Ra 0.8 as tested using a Mahr hand-held roughmeter, as shown in Fig. 14.

Finally, the finished products were tested for their performance in meshing on a worm drive testing platform (check whether the actual meshing area is consistent with the theoretical design), as shown in Fig. 15. During the meshing test,

the worm drive operated smoothly, showing no undesirable vibration, and the meshing contact spots were acceptable, thereby confirming that the products satisfied operating requirements.

6. Conclusions

This study developed a three-dimensional model for modifying the tooth profile of the Niemann worm wheel based on differential geometry and the working principle of gears. Compared with simulation modelling, this enveloping-based method of modelling yields more accurate models in a more time-efficient manner.

A technique for five-axis side milling of the Niemann worm wheel tooth flank was proposed: It used a tapered flat-end mill based on the working principle of gears and the numerical-control milling technology. The technique was confirmed feasible and valid through a simulation run by the VERICUT software.

The proposed technique was tested by machining Niemann worm wheels on a five-axis machine. The test demonstrates that the technique can not only resolve issues of low operating efficiency and cost efficiency inherent in point milling that used ball-end cutters but can also effectively guarantee machining surface quality. The technique offers great potential for applications in five-axis machining of other cylindrical worm drives, as well.

Acknowledgments

This work was supported by the National Natural Science Foundation of China (No. 51075347), Jiangsu Province Industry-University Research Prospective Joint Research Project (No. BY2015051-08), and Postgraduate Practice Innovation Program of Jiangsu Province (No. SJCX18_0347).

References

[1] J. Ruan, Q. Liu and F. Ruan, 3D parameterized design of worm- and- worm gear and its mechanis motion simulation analysing, *Machinery Design & Manufacture*, 11 (2007) 74-76.

[2] F. Zeng, M. Niu, X. Zhao and H. Yan, Three-dimensional simulation modeling for the worm wheel tooth surface, *Water Conservancy & Electric Power Machinery*, 29 (2007) 12-15.

[3] L. Zhi, L. Hong, W. Shaojun and Y. Guoming, Digitization modeling and CNC machining for cone-generated double-enveloping worm drive, *The International Journal of Advanced Manufacturing Technology*, 95 (2018) 3393-3412.

[4] Y. Cai, G. Xi, H. Fan, B. Wu and S. Wang, Tool-path planning for 5-axis numerical-control machining of arbitrary surface impeller, *Journal of Xi'an Jiaotong University*, 37 (1) (2003) 77-80.

[5] Y. Liang, D. Zhang, J. Ren, Z. C. Chen and Y. Xu, Accessible regions of tool orientations in multi-axis milling of blisks with a ball-end mill, *The International Journal of Advanced Manufacturing Technology*, 85 (5-8) (2016) 1887-1900.

[6] Q. Zou and J. Zhao, Iso-parametric tool-path planning for point clouds, *Computer-Aided Design*, 45 (2013) 1459-1468.

[7] L. Hong, L. Zhi and W. Shaojun, Digitization modeling and CNC machining for enveloping surface parts, *The International Journal of Advanced Manufacturing Technology*, 73 (1-4) (2014) 209-227.

[8] T. Wang, Z. Zhang, T. Wang, A. Xu, S. Hu and L. Zhao, High precision tool path planning algorithm for complex parametric surface, *Journal of Mechanical Engineering*, 43 (12) (2007) 109-113.

[9] B. Wu, M. Luo, Y. Zhang, S. Li and D. H. Zhang, Advance in tool path planning techniques for 5-axis machining of sculptured surfaces, *Journal of Mechanical Engineering*, 44 (2008) 9-18.

[10] J. Zhong, S. Mi and D. Yu, Research on algorithm of automatic generation of interference-free cutter location path for NC machining of freefrom surfaces with flat-end cutters, *Journal of Mechanical Engineering*, 35 (1999) 93-97.

[11] L. Li, G. Deng and C. Shang, Tool path optimization with high-efficiency and low energy consumption for surface CNC machining, *Journal of Machining Engineering*, 53 (2017) 184-194.

[12] S. Yan, Y. Zhou, X. Chen and X. Lai, Research on interference check and avoidance in five-axis NC machining, *China Mechanical Engineering*, 17 (2006) 1822-1825.

[13] F. Han, J. Wei, C. Zhang and X. Peng, Morphing technology for generating intermediate roughing models in multi-axis machining for complex parts, *Journal of Mechanical Science and Technology*, 33 (1) (2019) 315-322.

[14] S. Wang, *Meshing Principle of Cylindrical Worm Drive*, Tianjin University Press (1991).

[15] K. Wang, J. Wang, X. Deng, R. Zhu and Z. Xia, Study on meshing theory of the roller enveloping end face engagement worm drive, *Machine Design & Research*, 5 (2018) 89-91.

[16] O. B. Shamina, L. A. Belous and I. I. Ogol, Research on the optimal cutting parameters for ball end finish milling process of complex surfaces, *International Conference on Mechanical Engineering*, IEEE (2014).

[17] C. X. Yue, F. G. Yan, L. B. Li, H. Y. You and Q. J. Yu, Parametric design of ball-end milling tools for high speed milling, *Materials Science Forum*, 800-801 (2014) 484-488.

[18] B. R. C. Karuppanan and M. Saravanan, Optimized sequencing of CNC milling toolpath segments using metaheuristic algorithms, *Journal of Mechanical Science and Technology*, 33 (2) (2019) 791-800.

Quanping Sun is a Professor at Huaiyin Institute of Technology. His research interests include CAD/CAM and high-speed machining technology.

Haibing Wu is a Ph.D. in Mechanical Engineering. His research interests include gear CAD/CAM.

Zheng Zhang is a Master of Mechanical Engineering. His research interests include CAD/CAM and high-speed machining technology.